Appendix A: Extended source catalogues

Here we present the extended, multi-component source catalogues for the Abell 209 (Table A.1) and Abell S295 (Table A.2) cluster fields. (See the discussion in Sect. 5.3).

Table A.1. Extended sources in the Abell 209 MGCLS field.

(1) R.A. (deg)	(2) Dec. (deg)	(3) $S_{\rm int}$ (mJy)	(4) $\Delta S_{\rm int}$ (mJy)	(5) $I_{\rm peak}$ (mJy beam^{-1})	(6) LAS ($''$)	(7) Optical ID	(8) z
22.9860	−13.5807	6.049	0.053	2.411	70	-	-
23.0179	−13.6651	3.549	0.031	0.530	76	7190	0.2
22.8985	−13.4712	13.067	0.063	7.516	136	4968	0.27
23.1898	−13.3511	38.210	0.044	11.053	73	-	-
23.1666	−13.1819	3.503	0.040	1.367	56	6205	0.17
23.2199	−13.1328	2.074	0.066	0.807	54	8068	0.08
23.3709	−13.5798	1.993	0.029	0.716	54	1596	0.46
23.5330	−13.5719	2.742	0.030	1.061	82	WISEA J013407.92−133418.8	-
22.9890	−13.7451	3.618	0.056	1.742	107	4559	0.2
22.5779	−13.8580	0.855	0.016	0.563	37	591	0.36
22.5694	−13.8677	1.383	0.024	0.271	43	-	-
22.7784	−13.0524	26.687	0.125	4.139	94	WISEA J013106.83−130308.7	-
22.7566	−13.3371	1.705	0.023	0.441	54	1353	0.34
22.6263	−13.4913	26.158	0.029	16.544	76	4158	0.3
23.4957	−13.2933	3.019	0.027	0.767	89	WISEA J013358.96−131736.1	0.1
22.5028	−13.5075	1.689	0.033	0.430	115	-	-
23.3231	−13.6783	1.387	0.032	0.356	72	-	-
23.0368	−13.3279	8.527	0.026	4.004	68	WISEA J013208.83−131940.4	-
22.9934	−14.1088	4.678	0.027	0.286	74	WISEA J013158.40−140631.7	-
22.9494	−13.9215	6.061	0.019	2.928	33	WISEA J013147.85−135517.5	-
23.3539	−13.3721	1.959	0.019	0.838	94	-	-
22.6013	−13.1741	1.300	0.021	0.889	44	WISEA J013024.30−131026.7	-
23.3064	−13.0585	79.000	0.083	18.792	468	WISE J013313.50−130330.5	-
22.5031	−13.4747	13.570	0.016	7.594	58	WISEA J013000.74−132828.9	-
23.5757	−13.9423	6.193	0.028	1.196	93	WISEA J013418.18−135632.2	-
23.5998	−13.5860	1.831	0.012	0.827	41	WISEA J013423.94−133509.6	-
22.4480	−13.2866	28.055	0.026	8.629	65	-	-
23.5316	−13.8162	25.822	0.019	10.615	47	WISEA J013407.58−134858.4	-
22.9680	−13.6162	20.589	0.049	12.144	83	164	0.18
23.4633	−13.6041	2.668	0.018	0.857	40	-	-
22.6359	−13.8971	4.942	0.013	3.103	35	WISEA J013032.61−135349.6	-
22.6052	−14.0115	1.900	0.029	0.327	182	WISEA J013025.31−140042.5	-
22.9408	−13.6772	0.497	0.013	0.127	46	6812	0.19

Notes. Cols: (1–2) Source J2000 R.A. and Dec. – the position is that of the optical host, or the flux-weighted centroid if no optical host is identified; (3–4) MeerKAT 1.28 GHz integrated flux density and its uncertainty; (5) MeerKAT 1.28 GHz peak brightness; (6) Largest angular size; (7) optical host identifier where known – number-only IDs are from DECaLS; (8) Optical host redshift.

Table A.2. Extended sources in the Abell S295 MGCLS field.

(1) R.A. (deg)	(2) Dec. (deg)	(3) $S_{\rm int}$ (mJy)	(4) $\Delta S_{\rm int}$ (mJy)	(5) $I_{\rm peak}$ (mJy beam^{-1})	(6) LAS ($''$)	(7) Optical ID	(8) z
41.0580	−53.0237	8.243	0.021	3.486	71	-	-
41.7923	−52.8463	1.945	0.068	0.865	315	WISEA J024710.13−525046.6	0.088
41.2710	−52.8090	2.298	0.035	0.314	94	-	-
41.4154	−52.9641	123.317	0.137	16.971	587	ESO 154−IG 011 NED01	0.096704
42.2267	−52.9842	3.624	0.098	0.590	330	2686	0.46
42.2926	−53.0489	3.934	0.063	0.380	257	-	-
41.3352	−53.1849	33.371	0.057	10.234	117	3827	0.04
41.3259	−53.2520	104.090	0.038	21.642	117	WISEA J024518.34−531505.3	-
41.6932	−53.2965	3.580	0.041	0.826	144	1325	0.32
40.9512	−53.5577	7.315	0.048	1.761	96	-	-
42.0530	−53.4280	6.453	0.103	0.936	179	-	-
41.1320	−53.2208	56.355	0.031	31.709	49	-	-
41.4107	−53.6220	9.437	0.035	2.679	91	-	-
42.0002	−52.9116	3.227	0.056	2.377	174	3545	0.01
40.5346	−53.1455	3.978	0.029	1.060	53	3924	0.44
40.6013	−52.7182	1.878	0.028	0.411	57	WISEA J024224.31−524305.4	-
41.2443	−52.6912	4.972	0.054	2.696	117	3616	0.16
41.6280	−52.4638	16.509	0.061	3.417	140	-	-
41.4335	−52.8585	2.895	0.020	0.989	39	WISEA J024543.99−525130.3	-
41.5287	−53.2896	1.414	0.030	0.284	79	-	-
41.5898	−53.3468	0.884	0.020	0.182	44	2MASS J02462155−5320505	0.052199
41.9143	−53.5935	33.835	0.092	9.708	160	WISEA J024739.42−533536.5	-
41.3321	−53.0510	3.002	0.023	1.725	36	1286	0.26
41.3598	−53.0172	1.030	0.007	0.125	28	-	-
40.4822	−53.3950	79.906	0.033	1.045	180	3502	0.51
41.3927	−52.7395	75.244	0.054	17.551	80	WISEA J024534.30−524422.1	-

Notes. Cols: (1–2) source J2000 R.A. and Dec. – the position is that of the optical host, or the flux-weighted centroid if no optical host is identified; (3–4) MeerKAT 1.28 GHz integrated flux density and its uncertainty; (5) MeerKAT 1.28 GHz peak brightness; (6) largest angular size; (7) optical host identifier where known – number-only IDs are from DECaLS; (8) optical host redshift.

Appendix B: Star-forming galaxy catalogue for Abell 209: SFR and radio–FIR

To carry out the environment-dependent studies discussed in Sect. 8.2, namely galaxy SFRs and the radio-FIR correlation in Abell 209, we needed to identify which of the MGCLS-detected sources belong to the cluster, remove AGN-dominated sources from that group, and calculate the SFR and the radio-FIR ratio. Here we discuss the details of these procedures and the creation of the Abell 209 star-forming galaxies catalogue being released as part of the DR1 products. This catalogue includes the SFRs and radio–FIR ratios for the cluster's star-forming galaxies used in the scientific analyses presented in Sect. 8.2. An excerpt of this catalogue is shown in Table B.1.

B.1. Cluster galaxy membership

We assigned cluster membership using a combination of spectroscopic, $z_{\rm s}$, and photometric, $z_{\rm p}$, redshifts, with the latter determined using the `zCluster` photometric redshift code (Hilton et al. 2021) and photometry from DECaLS (Dey et al. 2019). The CLASH-VLT (Annunziatella et al. 2016) and ACReS (Haines et al. 2015) spectroscopic datasets contain secure redshifts for 1256 and 345 galaxies in the Abell 209 field, respectively, with a combined total of 1425 unique galaxies. We define spectroscopic cluster member galaxies as those with peculiar radial velocities within $\pm 3\,\sigma_{\rm v}$ of the cluster redshift, where $\sigma_{\rm v} = 1320\,{\rm km\,s^{-1}}$ is the line of sight velocity dispersion (Annunziatella et al. 2016). Photometry-based cluster membership is defined as those galaxies with $|z_{\rm p} - z_{\rm c}| < 3\,\sigma_{\rm bw}(1 + z_{\rm c})$, where z_c is the cluster redshift of 0.206 and $\sigma_{\rm bw} = 0.03$ is the scatter in our photometric redshift residuals. This scatter is determined using a bi-weight scale estimate (Beers et al. 1990), and the residuals are calculated as $\Delta z/(1 + z_{\rm s})$, where $\Delta z = z_{\rm s} - z_{\rm p}$.

We obtained a final catalogue of 523 MGCLS-detected cluster members within the primary-beam-corrected field of view, with 98 members within R_{200}. We determine the amount of contamination in the photometric redshift sample using the 91 member galaxies with both spectroscopic and photometric redshifts[25]. We find that 16% of the members selected using photometric redshifts have spectroscopic redshifts outside the photometric redshift cut range, while 23% of the spectroscopically identified cluster galaxies are missed by the photometric redshift selection.

B.2. AGN contamination

To separate star-forming galaxies from AGN-dominated galaxies, we used the 'R90' WISE infrared-selection criteria by Assef et al. (2018) (see also Stern et al. 2012; Assef et al. 2013). These utilise only the WISE W1−W2 colour to identify AGN without a threshold that depends on the W2 band magnitude

[25] For galaxies that have both a spectroscopic and photometric redshift, inclusion as a cluster member is defined by the spectroscopic redshift.

(see Eq. (4) of Assef et al. 2018, which identifies AGN with 90% reliability). With this selection method, we classify 64 radio-detected cluster galaxies as AGN and remove them from the cluster member sample. This leaves a total of 459 MGCLS-detected star-forming cluster members within the primary-beam-corrected field of view (80 within R_{200}). Table B.1 presents an excerpt of the catalogue of star-forming cluster galaxies in Abell 209.

B.3. Radio-derived star-formation rates

To estimate the SFR from the radio luminosities we used the Bell (2003) relation (see also Karim et al. 2011) scaled to a Chabrier (2003) IMF:

$$\mathrm{SFR}\ (\mathrm{M_\odot\,yr^{-1}}) = \begin{cases} 3.18\times10^{-22}L, & L > L_\mathrm{c} \\ \dfrac{3.18\times10^{-22}L}{0.1+0.9(L/L_\mathrm{c})^{0.3}}, & L \le L_\mathrm{c}. \end{cases} \quad \text{(B.1)}$$

Here, $L = L_{1.4\,\mathrm{GHz}}$ is the radio luminosity in $\mathrm{W\,Hz^{-1}}$ derived from the MGCLS 1.28 GHz total flux density, using a power law scaling and assuming a non-thermal spectral index of −0.8 (Condon 1992). $L_\mathrm{c} = 6.4\times10^{21}\,\mathrm{W\,Hz^{-1}}$ is taken to be the typical radio luminosity of an L_* galaxy. Bell (2003) argued that galaxies with low luminosities could have their non-thermal emission significantly suppressed and therefore need to be separated from the population with higherpg luminosities. However, as only a small percentage (39/459) of the final sample have luminosities lower than L_c, we do notpg separate according to luminosity. We measure SFRs ranging between 1.2 and 432 $\mathrm{M_\odot\,yr^{-1}}$, within the range of knownpg values. Under the assumption that the radio emission is due to star formation, the median 5σ sensitivity limit corresponds topg $\mathrm{SFR}_{5\sigma} > 2\,\mathrm{M_\odot\,yr^{-1}}$, with 429/459 star-forming members with SFRs above this limit.

B.4. FIR cross-matching for radio–FIR correlation

In order to study the radio–FIR correlation in Abell 209, we first need to determine FIR flux densities for the cluster star-formingpg galaxies. We cross-match the catalogue of 459 star-forming members with the *Herschel* 100 μm catalogue[26]. This yielded 49 star-forming cluster galaxies with both 1.28 GHzpg and 100 μm flux densities. We use the log of the ratio of these two quantities to investigate evolution in the radio–FIR relation.pg The *Herschel* 100 μm flux densities for the 49 galaxies and associated radio–FIR ratio are provided in the Abell 209pg star-forming galaxies catalogue shown in Table B.1.

Table B.1. Excerpt of the SFR and infrared catalogue of star-forming cluster galaxies in Abell 209, used in the SFR and radio–FIR studies in this paper (Sects. 8.2.1 and 8.2.2, respectively). The full catalogue is available online.

(1) Source ID	(2)-(28) ...	(29) z_s	(30) z Source	(31) SFR ($\mathrm{M_\odot\,yr^{-1}}$)	(32) ΔSFR ($\mathrm{M_\odot\,yr^{-1}}$)	(33) relR	(34) $S_{100\,\mu\mathrm{m}}$ (mJy)	(35) $\Delta S_{100\,\mu\mathrm{m}}$ (mJy)	(36) $\log\left(\frac{S_{1.28\,\mathrm{GHz}}}{S_{100\,\mu\mathrm{m}}}\right)$	(37) $\Delta\log\left(\frac{S_{1.28\,\mathrm{GHz}}}{S_{100\,\mu\mathrm{m}}}\right)$
1649	...	-	none	4.925	0.932	3.030	-	-	-	-
1660	...	-	none	1.945	0.599	1.975	-	-	-	-
1665	...	0.21111	ACReS	1.541	0.442	1.136	11.217	3.709	−2.515	0.268
1687	...	0.1963	CLASH	6.434	0.512	1.059	30.443	4.890	−2.284	0.104
1691	...	0.2071	CLASH	4.395	0.493	1.234	22.711	6.400	−2.322	0.171
1706	...	-	none	3.301	0.953	2.263	-	-	-	-
1728	...	0.21197	ACReS	2.654	0.500	1.227	27.888	5.172	−2.630	0.162
1731	...	-	none	1.646	0.562	1.566	-	-	-	-
1732	...	0.17697	ACReS	4.664	0.510	1.781	-	-	-	-

Notes. The first column is an assigned source ID for the radio source. Column descriptions for columns (2)–(28) (not shown here) are the same as in the optical cross-match catalogue, described in Table 3. The additional columns are: (29) spectroscopic redshift; (30) catalogue from which the redshift was obtained; (31–32) SFR and uncertainty; (33) radius from the centre in units of R_{200}; (34–35) 100 μm flux density and uncertainty; (36–37) log of the ratio between the radio and FIR flux densities, and associated uncertainty.

[26] The PACS Point Source Catalogue from the NASA/IPAC Infrared Science Archive: https://irsa.ipac.caltech.edu/cgi-bin/Gator/nph-scan?submit=Select&projshort=HERSCHEL

Appendix C: Automated searches for interesting objects

The definition of an 'unusual' radio object is subjective and dependent on the science case of interest. In the search for radio galaxies of interest, several of which are presented in Sect. 7, the MGCLS dataset was small enough for human inspection. However, it took a significant amount of time, with all images inspected by several people and the final set of radio galaxies of interest determined after cross-checking the various choices. For future surveys, exhaustive human searches for unusual objects may be impossible. We therefore used the MGCLS to examine the efficacy of machine learning techniques to find atypical, interesting objects.

ASTRONOMALY (Lochner & Bassett 2021) is a machine learning framework designed to automatically detect anomalous (rare or unusual) objects in very large datasets. We ran ASTRONOMALY on 128 px × 128 px (160″ × 160″) cutouts around components from the PYBDSF source finding (see Sect. 5), using the same framework as Lochner & Bassett (2021). To compare our results with those from human inspection, we restricted our search to the cluster fields where we had visually identified at least one extended radio galaxy with complex and/or unusual morphology (approximately 40% of the full sample). For those fields, we centred cutouts on components that were classified as having two or more Gaussian components by PYBDSF, which resulted in 21,449 cutouts.

We used ASTRONOMALY's anomaly score to order the data from most to least anomalous, comparing this list with a selected set of 43 sources that were previously identified as 'interesting' by one or more team members. Cutouts of the top 10 scoring objects are presented in Fig. C.1. Of the 43 interesting objects, ASTRONOMALY detected 22 in the top 1% (210 objects) of the rankings. Forty out of 43 sources are found in the first 10% of the list, while the remaining three could not be distinguished from 'normal' sources. We note that the vast majority of the 210 most highly ranked sources[27] are actually visually quite similar to the selected 43. We conclude that ASTRONOMALY can be a useful tool for rapid searches of morphologically interesting objects in large catalogues of radio sources, from which more targeted manual searches can be made efficiently.

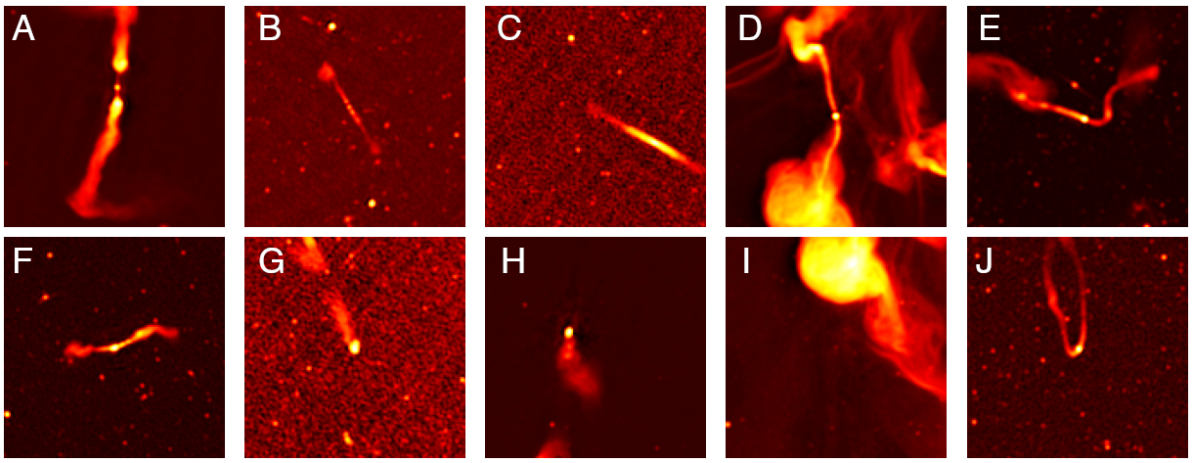

Fig. C.1. Ten top-ranked cutouts based on their ASTRONOMALY score. The cutouts are each 160″ per side, and their respective cluster fields (and cutout centres, in degrees of R.A., Dec.) are as follows: A: J0216.3−4816 (34.190, −47.836); B: J1423.7−5412 (214.984, −54.102); C: Abell 22 (5.055, −24.925); D: Abell 194 (21.502, −1.345); E: Abell S295 (41.422, −52.962); F: J0607.0−4928 (92.267, −48.900); G: Pandora (4.279, −29.934); H: J0216.3−4816 (33.252, −47.690); I: Abell 194 (21.522, −1.446); and J: J0738.1−7506 (114.851, −75.618). We note that sources *D* (and its extension to the south, identified as a separate source, *I*) and *J* are among the individual sources identified manually (independent of ASTRONOMALY) and selected for discussion in Sect. 7.

[27] Available at https://michellelochner.github.io/mgcls.astronomaly